Proceedings of ASME Turbo Expo 2004
2004 Power for Land, Sea, and Air
Vienna, Austria, June 14-17, 2004

GT2004-53195

NUMERICAL STUDY OF A CASCADE UNSTEADY SEPARATION FLOW

Zongjun Hu * **and GeCheng Zha** †
Department of Mechanical Engineering
University of Miami
Coral Gables, FL 33124

J. Lepicovsky ‡
QSS Group, Inc.
Cleveland, Ohio 44135

ABSTRACT

A CFD solver is developed to solve a 3D, unsteady, compressible *Navier-Stokes* equations with the *Baldwin-Lomax* turbulence model to study the unsteady separation flow in a high incidence cascade. The second order accuracy is obtained with the dual time stepping technique. The code is first validated for its unsteady simulation capability by calculating a 2D transonic inlet diffuser flow. Then a 3D steady state calculation is carried out for the cascade at an incidence of 10°. The surface pressure distributions compare reasonably well with the experiment measurement. Finally, the 3D unsteady simulation is carried out with 3 inlet Mach numbers at the incidence of 10°. The separation bubble oscillation and the static pressure oscillation on the leading edge of the blade suction surface exhibit clear periodicity. The details of the leading edge vortex shedding is captured. The inlet Mach number is shown to be the determinant factor in the characteristics of the separation flow. In the subsonic inlet flow region, increasing the inlet Mach number enlarges the separation region and the pressure oscillation intensity. The separation flow is weakened when the inlet flow becomes supersonic.

NOMENCLATURE

ρ density
μ, μ_t molecular, turbulent viscoscity
τ stress
γ specific heat ratio
ω vorticity
a local speed of sound
e energy per unit mass
l mixing length
p static pressure
u, v, w velocity components
x, y, z Cartesian coordinates
t time
C_p static pressure coefficient
E, F, G inviscid flux vector
Ma Mach number
Pr Prandtl number
Q conservative variable vector
Re Reynolds number
R, S, T viscid flux vector

Introduction

Flutter in axial turbomachines is a highly undesirable and dangerous self-excited blade oscillation mode that can result in high cycle fatigue blade failure. Modern turbine engines employ transonic fan stages with high aspect ratio blades that are prone to flutter. It is imperative to understand the origins of flutter for reliable and safe operation of these engines.

High subsonic and transonic torsional stall flutter occurs near the fan stall limit line at speeds up to about 80% of the design speed and with high incidence. Two potential factors are assumed to trigger the flutter mode, the shock wave motion in the transonic conditions and the large separation on the suction side of the blade surface under high incidence angle [1]. Actually, the shock wave does not appear until very high subsonic inlet Mach number is reached. However, the flutter exists in much

*PhD Student, Email: zongjunhu@yahoo.com
†Associate Professor, Director of CFD Lab
‡Senior Research Supervisor

wider Mach number region (appears in smaller Mach number) than where the shock wave exists. The separation flow on the leading edge of the blade suction side is a likely cause for flutter. A series of experiments have been carried out in NASA Glenn Research Center to study the transonic separation flow characteristics of modern airfoils for transonic fans. A low aspect ratio fan blade operating near the stall flutter boundary under high incidence is simulated in the NASA Transonic Flutter Cascade. The unsteady pressure is measured at selected points on the chord line of the cascade surfaces [2]. The flow pattern is visualized using dye oils and schilieren flow visualization methods [1].

The objective of this paper is to numerically study the unsteady characteristics of the NASA transonic cascade separation flow with a incidence angle of 10° in 3D condition. A CFD solver is developed to solve the 3D, unsteady, compressible *Navier-Stokes* equations with the *Baldwin-Lomax* turbulence model [3]. The dual time stepping method is applied to achieve the second order accuracy in time. The unsteady computing capability of the CFD solver is validated by a transonic inlet diffuser flow, where turbulent boundary layer interacts with the shock wave and causes unsteady flow separation. Finally, the unsteady separation flow simulation is carried out at 3 inlet Mach numbers, 0.5, 0.8 and 1.18. The vortex shedding mechanism is analyzed for the case of Mach number 0.5. The characteristics of the separation flow under varying inlet Mach numbers is demonstrated.

Numerical Algorithm

The governing equations for flow field simulation used in this paper are the *Reynolds* averaged time-dependent compressible *Navier-Stokes* equations in generalized coordinate system. The simulation is carried out with finite volume method. The equations are discretized using the third order MUSCL differencing [4]. The linearized equation systems are solved using the *Gauss-Seidel* line iteration. Upwind differencing is implemented with the *Roe* scheme [5] and the *van Leer* scheme [6]. The second order accuracy of time marching is obtained with the dual time stepping technique.

Governing Equations

For simplicity, the non-dimensional form of the equations in conservation law form are expressed in *Cartesian* coordinates as the followings.

$$\frac{\partial Q}{\partial t}+\frac{\partial E}{\partial x}+\frac{\partial F}{\partial y}+\frac{\partial G}{\partial z}=\frac{\partial R}{\partial x}+\frac{\partial S}{\partial y}+\frac{\partial T}{\partial z} \qquad (1)$$

where

$$Q=[\bar{\rho},\bar{\rho}\tilde{u},\bar{\rho}\tilde{v},\bar{\rho}\tilde{w},\bar{\rho}\tilde{e}]^T$$

$$E=[\bar{\rho}\tilde{u},\tilde{p}+\bar{\rho}\tilde{u}^2,\bar{\rho}\tilde{u}\tilde{v},\bar{\rho}\tilde{u}\tilde{w},(\bar{\rho}\tilde{e}+\tilde{p})\tilde{u}]^T$$

$$F=[\bar{\rho}\tilde{v},\bar{\rho}\tilde{u}\tilde{v},\tilde{p}+\bar{\rho}\tilde{v}^2,\bar{\rho}\tilde{v}\tilde{w},(\bar{\rho}\tilde{e}+\tilde{p})\tilde{v}]^T$$

$$G=[\bar{\rho}\tilde{w},\bar{\rho}\tilde{u}\tilde{w},\bar{\rho}\tilde{v}\tilde{w},\tilde{p}+\bar{\rho}\tilde{w}^2,(\bar{\rho}\tilde{e}+\tilde{p})\tilde{w}]^T$$

$$R=\frac{1}{Re}[0,\bar{\tau}_{xx},\bar{\tau}_{xy},\bar{\tau}_{xz},\beta_x]^T$$

$$S=\frac{1}{Re}[0,\bar{\tau}_{xy},\bar{\tau}_{yy},\bar{\tau}_{yz},\beta_y]^T$$

$$T=\frac{1}{Re}[0,\bar{\tau}_{xz},\bar{\tau}_{yz},\bar{\tau}_{zz},\beta_z]^T$$

The shear stress terms are expressed as,

$$\bar{\tau}_{ij}=-\frac{2}{3}(\tilde{\mu}+\mu_t)\frac{\partial \tilde{u}_k}{\partial x_k}\delta_{ij}+(\tilde{\mu}+\mu_t)\left(\frac{\partial \tilde{u}_i}{\partial x_j}+\frac{\partial \tilde{u}_j}{\partial x_i}\right)$$

$\beta_x,\beta_y,$ and β_z are expressed as,

$$\beta_i=(\tilde{\mu}+\mu_t)\tilde{u}_j\tau_{ij}+\frac{1}{\gamma-1}\left(\frac{\tilde{\mu}}{Pr}+\frac{\mu_t}{Pr_t}\right)\frac{\partial \tilde{a}^2}{\partial x_i}$$

In above equations, ρ is the density, u, v, w are the *Cartesian* velocity components in x, y, z directions, p is the static pressure, and e is the energy per unit mass, a is the local speed of sound. The overbar $\bar{}$ denotes a *Reynolds* average, and the tilde $\tilde{}$ is used to denote the *Favre* mass average. The molecular viscosity μ is determined by the *Sutherland* law. The *Reynolds* stresses are related to mean flow variables through a turbulent viscosity μ_t based on the *Boussinesq* assumption, and the turbulent viscosity μ_t is determined by the *Baldwin-Lomax* model [3].

Baldwin-Lomax Turbulence Model [3]

The turbulent viscosity μ_t is computed separately in two layers. For clarity, the overbar and tilde are omitted in the following.

At inner layer,

$$\mu_{ti}=\rho l^2|\omega| \qquad (2)$$

where

$$l = ky\left[1-\exp\left(-\frac{y^+}{A^+}\right)\right] \tag{3}$$

ω is the local vorticity, y and y^+ are the dimensional and dimensionless distance to the wall.

At the outer layer,

$$\mu_{to} = KC_{\text{cp}}\rho F_{\text{wake}}F_{\text{kleb}} \tag{4}$$

$$F_{\text{wake}} = \min\left(y_{\max}F_{\max}, C_{\text{wake}}y_{\max}u_{\text{diff}}^2/F_{\max}\right)$$

$$F_{\text{kleb}} = \left[1+5.5\left(\frac{C_{\text{kleb}}y}{y_{\max}}\right)^6\right]^{-1}$$

In the above formulations, k, A^+, C_{wake}, C_{kleb}, C_{cp} and K are constants.

The quantities u_{diff}, $F_{\max}$ and $y_{\max}$ are determined by the velocity profile following a line normal to the wall. $F_{\max}$ and $y_{\max}$ are the maximum value and the corresponding distance of function F_y,

$$F_y = y|\omega|\left[1-\exp\left(-\frac{y^+}{A^+}\right)\right] \tag{5}$$

$$u_{\text{diff}} = \left(\sqrt{u^2+v^2+w^2}\right)_{\max} - \left(\sqrt{u^2+v^2+w^2}\right)_{\min} \tag{6}$$

In the 3D computation of this paper, the wall is located at the 4 side of the computation domain. The value of μ_t is simply computed according to the closest wall surface. $F_{\max}$ and $y_{\max}$ is searched from the wall to the center of the passage. In the wake region, the exponential part is set to zero in Eq. (3) and Eq. (5). The second part of Eq. (6) is zero outside of the wake region. All constants are assigned the standard values suggested in [3].

The turbulence model is applied and validated in [7] for a subsonic turbulent flat plate boundary layer flow.

Discretization Method

The governing equations (1) are discretized and solved using finite volume method. The equations are rewritten as,

$$\frac{\partial Q}{\partial t} = -\frac{\partial(E-R)}{\partial x} - \frac{\partial(F-S)}{\partial y} - \frac{\partial(G-T)}{\partial z} \tag{7}$$

Using finite volume method,

$$\frac{\partial Q}{\partial t}\cdot \mathrm{d}V = -\int_s R_F \cdot s$$

where, dV is the volume of cell, s is cell interface area vector in the normal outward pointing direction, and,

$$R_F = (E-R)\,i + (F-S)\,j + (G-T)\,k$$

Discretize this equation in implicit form with first order differencing in both time and space. The discretized equations at cell (i,j,k) are written as the following,

$$\begin{aligned}\Delta Q + A^+\Delta Q_{i-1} + A\Delta Q + A^-\Delta Q_{i+1} \\ +B^+\Delta Q_{j-1} + B\Delta Q + B^-\Delta Q_{j+1} \\ +C^+\Delta Q_{k-1} + C\Delta Q + C^-\Delta Q_{k+1} = R\end{aligned} \tag{8}$$

where,

$$R = \frac{\Delta t}{\mathrm{d}V}\left(-\int_s R_F\cdot \mathrm{d}s\right)^n$$

$$\Delta Q = Q^{n+1} - Q^n$$

where, n, $n+1$ denote two sequential time steps.

Equation (8) is solved using the line *Gauss-Seidel* iteration method. The convective fluxes E, F, G are evaluated by the *Roe* scheme [5] or the *van Leer* scheme with *MUSCL* differencing. Third order differencing is used for convective terms E, F, G and second order central differencing is used for the viscous terms R, S, T. Local time step is applied to speed up the convergence.

Time Marching

The dual time stepping technique is used to obtain the second order accuracy in time. The method is made possible by

adding a pseudo temporal term $\frac{\partial Q}{\partial \tau}$ to Eq. (1). The governing equation becomes,

$$\frac{\partial Q}{\partial \tau} + \frac{\partial Q}{\partial t} = -\frac{\partial (E-R)}{\partial x} - \frac{\partial (F-S)}{\partial y} - \frac{\partial (G-T)}{\partial z} \quad (9)$$

where τ is the pseudo time and t is the real time.

The real time step Δt is specified by the physical time interval. The solution iteration is operated on the pseudo time step $\Delta\tau$, which is limited by the CFL criterion. When the implicit solution is converged on pseudo time $\Delta\tau$ iteration, one physical time step Δt is finished. Numerical techniques, such as local time step, *Gauss-Seidel* method, can still be used to speed up the convergence in the iteration on the pseudo time step $\Delta\tau$.

Write Eq. (1) in integral form,

$$\frac{\partial Q}{\partial \tau} + \frac{\partial Q}{\partial t} = R \quad (10)$$

Applying the second order discretization for $\frac{\partial Q}{\partial t}$,

$$\frac{\partial Q}{\partial t} = \frac{3Q^{n+1} - 4Q^n + Q^{n-1}}{2\Delta t}$$

where n is the physical time step. The value at time step $n+1$ is unknown and will be solved by the pseudo time iteration.

At the unknown time step $n+1$, using *Euler* discretization for the pseudo temporal term, let m and $m+1$ be consequential pseudo time steps.

$$\frac{\partial Q}{\partial \tau} = \frac{Q^{n+1,m+1} - Q^{n+1,m}}{\Delta \tau}$$

The governing equations with pseudo temporal term Eq. (10) are implicitly written as,

$$\frac{Q^{n+1,m+1} - Q^{n+1,m}}{\Delta\tau} + \frac{3Q^{n+1} - 4Q^n + Q^{n-1}}{2\Delta t} = R^{n+1,m+1} \quad (11)$$

Therefore,

$$\left[\left(\frac{1}{\Delta\tau} + \frac{1.5}{\Delta t}\right) I - \left(\frac{\partial R}{\partial Q}\right)^{n+1,m}\right] \delta Q^{n+1,m+1} = R^{n+1,m} - \frac{3Q^{n+1,m} - 4Q^n + Q^{n-1}}{2\Delta t} \quad (12)$$

Eq. (12) is iteratively solved using the *Gauss-Seidel* line iteration methods. $Q^{n+1,m}$ is assumed to be equal to Q^n at the beginning of the iterations.

Results and Discussion

In this section, the unsteady simulation of the code is first validate by a transonic inlet-diffuer flow. Then the numerical study is carried out for the casecade separated flow with an incidence angle of 10° under 3 inlet Mach numbers, 0.5, 0.8 and 1.18. The cascade experiment measurement is reported in [2, 8].

Unsteady Transonic Inlet-diffuser Simulation

A 2D transonic inlet-diffuser internal flow is first calculated to validate the unsteady simulation ability of the current code. This case is experimentally measured in [9] to study the frequency characteristics of shock wave oscillation resulting from the interaction between the turbulent boundary layer and the shock wave. The test section is designed to obtain a 2D flow condition. The flow enters the inlet diffuser under subsonic condition and accelerates to supersonic at the throat. By adjusting the back pressure level at outlet, different shock wave structures are obtained.

Fig. 1 shows the the mesh structure. The inlet diffuser has a height of h_t =4.4 cm at the throat and a total length of $12.6h_t$. The inlet height is $h_{in} = 1.4h_t$. The mesh size is $130(x)\times60(y)$. The grid is uniformly distributed in horizontal direction before and after the throat section. In the throat region, the grid is clustered to catch the shock wave sharply. The mesh is also clustered close to the upper and bottom walls to make sure the maximum y^+ is below 3. The *Roe* scheme is applied to evaluate the control volume inter surface flux.

The total pressure p_t, total temperature T_t and flow angle α are specified at the inlet. The no-slip adiabatic boundary condition is applied at top and bottom walls. The back pressure level is set as p_{outlet}/p_t =0.72 as the experiment. The throat height is used as the characteristic length. The *Reynolds* number is 4.3896×10^5. The static pressure is fixed at the outlet. The physical time step is set as 0.28272 ms, which is about 7% of the shock oscillation cycle. The *Gauss-Seidel* solution is carried out between two sequential physical time steps with a CFL of 5.0. The converged solution for each physical time step is obtained after 50 pseudo time step iterations. The obtained inlet Mach number is 0.458.

The instant Mach contours are shown in Fig. 2. The shock wave is clearly captured. The flow is separated after the shock, which brings high unsteadiness to the flowfield. The location of the shock wave moves back and forth downstream of the throat region. The flow field parameters, including the shock wave location and static pressure, vary periodically with time in the region after the shock wave. Fig. 3 shows the pressure oscillation

history on the upper wall at outlet. More clear frequency information is revealed using the Fast Fourier Transform (FFT) technique. The static pressure frequency spectrum is shown in Fig. 4 on the left compared with experiment measurement based on the shock wave motion [9] on the right. The computed frequency spectrum peak is at 250 Hz, which is close to the experiment measurement frequency, 200 Hz. The reason for the discrepancy between the computational and experimental results may be the inadequacy of the turbulence model, which will affect the boundary layer thickness and hence the shock motion.

3D Cascade Geometry, Meshing and Boundary Conditions

The test section of the NASA transonic flutter cascade facility is shown in Fig. 5. Nine blades were located in the test section. With a reference to the axial direction, the setting angle of the inlet duct is 20°, and the blade-setting angle is 30°. This results in 10° chordal incidence for the airfoils. Fig. 6 shows the mid-span cross section of the cascade. The test section has a rectangular cross section of 5.84 cm wide (pitch s) by 9.59 cm high (height h). The aerodynamic chord c is 8.89 cm with a maximum thickness of $0.048c$ at $0.625c$ from the leading edge. This results in a solidity c/s of 1.52. The experiment blades have constant cross section in span-wise direction, except near the end walls, where they have large, diamond-shaped fillets to support the attachment shafts. The blades are not exactly symmetric about the mid-span plane. The fillet on the drive-side is larger than the one on the free side (Fig. 9). This makes the 3D calculation necessary.

The current simulation is carried for the pitch-wise central passage of the cascade. The cascade shows good periodicity in flowfield measurement [10]. The mid-span computational domain is shown in Fig. 7. In the plot, to make x axis pointing to right horizontally, the blade is rotated 90° counter-clockwise relative to Fig. 5 and 6. This is followed by the rest figures in this paper. To minimize the influence of boundary condition specification, the computation domain is stretched outside for 1.2 chord length in stream-wise direction at inlet and outlet. Boundaries, $A-B$, $C-D$, $E-F$ and $G-H$ are set as periodic boundaries. No-slip adiabatic boundary condition is applied at the wall surface $B-C$ and $F-G$. Total pressure P_t, total temperature T_t and flow angles α, β are given at inlet boundary $A-H$ uniformly. At the outlet boundary $D-E$, a constant static pressure is fixed. The no-slip adiabatic boundary condition is also applied on the two end walls at bottom and top. The general coordinates is used in the simulation with ξ axis aligning with the stream-wise direction, η axis aligning with the pitch-wise direction and ζ axis following the span-wise direction.

The three dimensional mesh structure is shown in Fig. 8. The end walls are located at the bottom and the top. The mesh size is $100(\xi)\times60(\eta)\times60(\zeta)$. In ξ direction, there are 15, 70 and 15 mesh points allocated before, on and after the blade surface. Fig. 9 shows the the mesh structure and the geometry of the blade at bottom, mid-span and top planes. The mesh is clustered in regions close to the blade surface on the η direction and in regions close to the top and the bottom end walls in the ζ direction. In ξ direction, the mesh is clustered in regions close to the leading and trailing edges of the blade, where the flow structure is complicated. The maximum y^+ at all wall boundaries is under 3. For clarity, every one of two grids lines are plotted in Fig. 8 and Fig. 9.

Steady state results

Though the flow is separated and unsteady when the incidence is high, the time averaged flow field is calculated with the local time stepping enabled and the dual time stepping disabled in the code. The solution is obtained when the calculated flowfield is unchanged. The steady state solution is also used as the initial solution for the corresponding unsteady calculation.

An incidence of 10° is chosen for the following numerical study. The *van Leer* scheme is used to evaluate the inviscid flux. Though the *van Leer* scheme is more diffusive than the *Roe* scheme, when working with the *Baldwin-Lomax* turbulence model, it gives better agreement with the experiment in the current code. The *Roe* scheme predicts the separation larger than the experiment. The inlet Mach number is obtained by adjusting the back pressure level.

The result of the case with inlet Ma=0.5 is described in this section to demonstrated the characteristics of the 3D separation flow field. More results for Ma=0.8 and Ma=1.18 can be found in [7]. In the case of Ma=0.5, the corresponding *Reynolds* number is 9.6699×10^5. The CFL in the *Gauss-Seidel* iteration is 5.0. The calculation starts from a flowfield at rest.

The flow stream lines on the mid-span plane is shown in Fig. 10. The flow exhibits a large separated region on the suction surface that starts immediately at the leading edge and extends down to 45% of the blade chord. The flow pattern on the suction surface is plotted on the left in Fig. 11. The separation region has a parabola shape, which is approximately symmetric about along the blade mid-span line and extends to the blade upstream corners. Two counter rotating vortexes are formed downstream of the blade leading edge corners on the suction surface at its two ends. The experiment visualization with dye oil technique is shown in Fig. 11 on the right. The computation results agree with the experiment fairly well, except that the numerical results shows a fuller separation region in span-wise direction.

The mid-span static pressure distribution is plotted and compared with the experiment measurement in Fig. 12. A reasonable agreement is achieved. The pressure is expressed as the pressure

coefficient,

$$C_p = \frac{p - p_{in}}{\frac{1}{2}\rho_{in} U_{in}^2}$$

where p is the local static pressure. p_{in}, ρ_{in} and U_{in} are the averaged static pressure, density and velocity at the inlet.

On the leading edge of the suction side, the numerical pressure results varies more steeply than that given by the measurement. The separation region denoted by the cross of the pressure distributions on suction and pressure surfaces agrees very well with the experiment.

The separation region is enlarged when *Roe* scheme is used to calculate the inviscid flux. A possible reason for the difference is the application of turbulence model on the H-type mesh in the current code. It is shown that the implementation details the *Baldwin-Lomax* model is vital to the resulted turbulent viscosity accuracy. Better agreement is obtained in [11] for the same case, where the *Roe* scheme is applied on an O-type mesh. The H-type mesh in the current code is generated by an elliptic method as a whole, which meets difficulty in the mesh orthogonality in the wall boundary region, which affects the accuracy in calculating the outer layer eddy viscosity coefficient. A two-layer H-type mesh is used in [12], where an inner algebraic mesh is surrounded by an outer elliptic method generated mesh. The the inner mesh is designed to achieve better orthogonality. These grid generation techniques will be implemented in the code in the next step research work.

Unsteady separated flow simulation

The separation is believed to bring high unsteadiness to the cascade flow pattern. The inlet Mach number is an important factor which affects the separation characteristics [7]. To study the influence of the inlet Mach number on the unsteady characteristics of the separated flow, numerical simulation is carried out for high incidence angle cases with Mach number 0.5, 0.8 and 1.18. Each unsteady calculation is carried out based on its corresponding steady state result.

Due to the limitation of the computation capability, the physical time interval is chosen as large as 10% of the characteristic time of the cascade, $t_c = c/U_{in}$. $U_{in}$is the inlet velocity. This time interval varies with the inlet Mach number. The CFL number used in the pseudo time *Gauss-Seidel* implicit iteration is 20.0. Twenty pseudo time steps are used for each physical time step. Two parameters are recorded to analyze the unsteady characteristics of the separation flow. The first is the mid-span separation bubble length(x), which is marked by the streamwise zero velocity point at the first inner mesh point on the suction surface. The second parameter is the unsteady static pressure (p) measured at the location of 13% downstream the leading edge on the suction surface, which is the same as the experiment measurement location. The unsteady pressure is refered as "check point pressure" in the following.

Ma = 0.5 In the case of Ma = 0.5, the physical time interval is set as 0.052744 ms.

Fig. 13 shows the time history of the separation length oscillation in a time segment of 16 ms ($30t_c$). The separation length increases rapidly from $0.45c$ to $0.66c$ in the first 1.63 ms ($3t_c$) and then decreases to $0.63c$ at t =2 ms ($3.8t_c$). The separation region then grows up again toward downstream to $0.73c$ at t =3 ms ($5.7t_c$). With the time progressing, the separation region boundary oscillates back and forth on the suction surface. The average length tends to increase gradually until a periodic state is reached after 4.4 ms ($8.3t_c$). The oscillation of the separation length is between $0.73c$ and $0.76c$ with a fixed cycle. The periodicity information is clearly extracted using the FFT technique. The separation region oscillation spectra is calculated from the unsteady data after 4.4 ms ($8.3t_c$). The frequency spectrum is shown in Fig. 14, which clearly shows a peak at 770 Hz. This indicates the separation length oscillates with a period of 1.25 ms ($2.37t_c$).

Compared with the steady state solution, the unsteady separation calculation results in larger separation size. The reason is not clear.

The unsteady check point pressure data shows similar characteristics of the unsteady separation flow. Fig. 15 shows a segment of 16 ms ($30t_c$) pressure oscillation data. The pressure start at p =2.659 from the steady state results. The oscillation is between p =2.68 and p =2.72 after t =4.4 ms ($8.3t_c$). The oscillation amplitude is about 1.5% of the averaged pressure level. The frequency spectrum is shown in Fig. 16 with a peak at 770 Hz.

The mechanism behind the unsteady characteristics of the separation is illustrated in Fig. 18, where the evolution of a separation oscillation cycle is plotted. The stream lines at 8 time steps show the leading edge vortex shedding development. There are 4 physical time steps (0.21 ms, $0.4t_c$) between 2 sequential plots. The relationship between the oscillation of the pressure and the separation length is shown in Fig. 17.

At the starting time level a (t =4.4305 ms, $8.4t_c$), the separation region has just passed the maximum length location. There are 2 vortexes in the separation bubble. They are rotating in the same direction. The check point pressure is going up. At time level b (t =4.6415 ms, $8.8t_c$), the two vortexes are pushed toward downstream. The second vortex diminishes. The first vortex grows quickly and becomes the only vortex in the separation bubble. The separation region becomes thicker in the span-wise direction, but shorter in the stream-wise direction. The surface check point pressure reaches its maximum level at this time level. At time level c (t =4.8524 ms, $9.2t_c$), the separation bubble approaches its shortest length in stream-wise direction, and maximum thickness in the span-wise direction. The check point pres-

sure is going down. At time level *d* (t = 5.0634ms, 9.6t_c), the separation bubble has passed the minimum length location, and begins to extend toward downstream. The check point pressure is still going down. At time level *e* (t =5.2744 ms, 10.0t_c), a new vortex is generated at leading edge and becomes the first vortex. The check point pressure reaches its minimum value. The separation length is still increasing. At time level *f* (t=4854 ms, 10.4t_c), the first vortex continues to grow. The second vortex is pushed toward downstream. Both the check point pressure and the separation length are going up. The latter is approaching its maximum location. At time level *g* (t =5.6964 ms, 10.8t_c), the two vortexes have almost the same size, the flow structure is close to the starting time level *a*. The separation boundary has passed its maximum location and begin to shrink toward upstream. The check point pressure is going up. At time level *h* (t =5.9073 ms, 11.2t_c), the second vortex diminishes. A new cycle is started at this time level.

The leading edge vortex shedding exhibits obvious periodical pattern in its evolution process. The leading edge keeps generating new vortexes. The new vortex pushes the old vortex bubble toward downstream and the old vortex decreases in size at the same time. When the two vortexes become of the same size, the maximum separation length is reached, where the separation bubble has the thinnest size in span-wise direction. As the new vortex grows further, the old vortex will diminish. The separation bubble will move upstream and makes the bubble thicker. The leading edge surface check point pressure reaches its maximum level when the separation bubble shrinks and reaches its minimum level when the separation bubble boundary extends. The vortex generation, pressure variation and separation length oscillation have the same frequency characteristics with a phase difference as shown in Fig. 17. Such oscillation is maybe one of the reasons to cause to flutter.

Ma = 0.8 The physical time interval used in the calculation for the case of *Mach* number 0.8 is 0.0342 ms. A similar flowfield unsteady characteristics is exhibited in the computation results.

Fig. 19 and Fig. 21 show the separation length and the checkpoint static pressure oscillation history in a time period of 21 ms. A clear periodicity is shown in these two figures. It is found in the time averaged steady state study in [7] that, the increase of the inlet Mach number will enlarge the separation bubble in size. Fig. 21 indicates that the inlet Mach number increase also increases the amplitude of the pressure oscillation. The oscillation amplitude is increased to about 5% of the averaged pressure level. The increased kinetic energy in the inflow bring higher unsteadiness intensity to the separated flow filed.

The corresponding FFT frequency analysis is shown in Fig. 20 and Fig. 22 respectively. The frequency analysis is based on the oscillation data after t=5 ms. The unsteady separation flow exhibits higher oscillation frequency because of the increased inlet Mach number. A clear frequency spectrum peak is shown at 1400 Hz in both figures, twice the frequency in the case of Ma = 0.5.

Ma = 1.18 In the steady state simulation of the cascade at *Ma*=1.18 in [7], the separation flow characteristics are very different from those at subsonic. The further increased kinetic energy in the inflow makes the flow attached to the blade surface in the leading edge. A smaller sized separation region appears after the shock wave because of the interaction of the shock wave and the turbulent boundary layer. The separation bubble shrinks in size and is located only in a small region at the center of the suction surface region.

The physical time interval in the calculation is set as 0.02483 ms. The pressure check point is located outside of the separation region in the supersonic case. The pressure oscillation history is shown in Fig. 23. The oscillation amplitude is very small compared to the cases of Ma = 0.5 and Ma = 0.8. The flow tends to steady at the leading edge. The pressure oscillation frequency spectrum is shown in Fig. 24.

The computed characteristics of the separation flow above is similar to the experiment measurement in [2]. In [2], when the blade is fixed, the blade surface pressure for low subsonic inlet flow at *Ma*=0.5 and low supersonic inlet flow at *Ma*=1.1 exhibits very low unsteadiness and very strong self-induced oscillations with a frequency of 110Hz is observed in high subsonic inlet flow at *Ma*=0.8. However, the strong low frequency oscillation is attributed to the tunnel resonance characteristics instead of the flow unsteadiness due to the flow separation in [8]. Even though, the cascade flow separation is believed to have a direct relation with the wall surface pressure unsteady oscillation, which is an important factor to the flutter. Futher detailed numerical research is necessary to discover the mechanism.

Conclusions

A 3D unsteady compressible *Navier-Stokes* solver is developed in this paper to numerically study the unsteady characteristics of the separation flow in a transonic flutter cascade under a high incidence angle of 10°. The dual time stepping method is applied to achieve the second order accuracy time marching. The linearized governing equation system is solved by the *Gauss-Seidel* line iteration method. The *Baldwin-Lomax* model is used to simulate the turbulence effects. The following conclusions are drawn from this study.

1. The high incidence cascade separation flow shows a sinusoidal pattern on the oscillation of the surface pressure and the separation bubble size. A frequency spectrum peak is obtained at 770Hz for the case of *Ma*=0.5 and 1400Hz for the case of *Ma*=0.8.

2. The leading edge vortex shedding is the mechanism behind the unsteady characteristics of the subsonic high incidence separation flow. New vortexes are continuously generated at the suction surface leading edge. The new vortex grows and pushes the old vortexes downstream. The interaction between the vortexes results in the periodical oscillation of the separation bubble size and the surface pressure. The vortex generation, pressure variation and separation length oscillation have the same frequency characteristics with a phase difference.
3. The characteristics of the separation flow is determined by the inlet Mach number. When the inlet flow goes from lower subsonic to higher subsonic, the size and the oscillation intensity of the separation bubble are enhanced. The flowfield oscillation peak frequency increases. When the inflow goes further to supersonic, the flow is attached on the leading edge. A small size separation bubble due to the interaction of the shock wave and the turbulent boundary layer is located right after the shock wave.

Acknowledgement

This work is partially supported by AFOSR Grant F49620-03-1-0253 monitored by Dr. Fariba Fahroo.

REFERENCES

[1] Lepicovsky, J., Chima, R. V., Jett, T. A., Bencic, T. J., and Weiland, K. E., 2000. "Investigation of flow separation in a transonic-fan linear cascade using visualization methods". *NASA/TM-2000-210521* Dec. .

[2] Lepicovsky, J., McFarland, E. R., Capece, V. R., and Hayden, J., 2002. Unsteady pressures in a transonic fan cascade due to a single oscillating airfoil. ASME Paper GT-2002-30312.

[3] Baldwin, B. S., and Lomax, H., 1978. "Thin layer approximation and algebraic model for separated turbulent flows". *AIAA Paper 78-257* .

[4] Leer, B. V., 1977. "Towards the ultimate convservative difference scheme, III". *Jouranl of Computational Physics,* **23** , pp. 263–75.

[5] Roe, P., 1981. "Approximate Riemann solvers, parameter vectors, and difference schemes". *Journal of Compuational Physics,* **43** , pp. 357–72.

[6] van Leer, B., 1982. "Flux-vector splitting for the Euler equations". *Lecture Note in Physics,* **170** .

[7] Hu, Z., Zha, G., and Lepicovsky, J., 2004. Numerical study on flow separation of a transonic cascade, Jan. AIAA Paper 2004–0199.

[8] Lepicovsky, J., Capece, V. R., and Ford, C. T., 2003. Resonance effects in the NASA transonic flutter cascade facility. ASME Paper GT-2003-38344.

[9] Bogar, T. J., Gajben, M., and Kroutil, J. C., 1981. "Characteristic frequency and lengh scales in transonic diffuser flow oscillations". *AIAA Paper 81-1291* .

[10] Lepicovsky, J., McFarland, E. R., Chima, R. V., and Wood, J. R., 2000. "On flowfield periodicity in the nasa transonic flutter cascade, part I — experimental study". *NASA/TM-2000-209934* Mar. .

[11] Grüber, B., and Carstens, V., 2001. "The impact of viscous effects on the aerodynamic damping of vibrating transonic compressor blades—a numerical study". *Journal of Turbomachinery,* **123** .

[12] Weber, S., and Platzer, M. F., 2000. "A Navier-Stokes analysis of the stall flutter characteristics of the Buffum cascade". *Journal of Turbomachinery,* **122** .

[13] Lepicovsky, J., McFarland, E. R., Capece, V. R., Jett, T. A., and Senyitko, R. G., 2002. "Methodology of blade unsteady pressure measurement in the nasa transonic flutter cascade". *NASA/TM–2002-211894* Oct. .

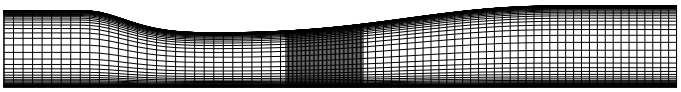

Figure 1. Transonic inlet diffuser computation mesh

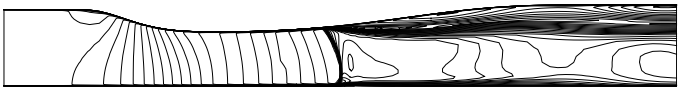

Figure 2. Transonic inlet diffuser Mach contour

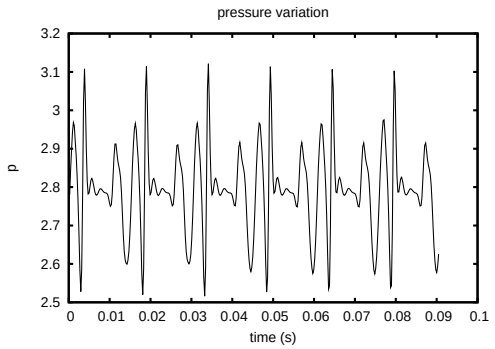

Figure 3. Transonic inlet diffuser outlet wall pressure variation

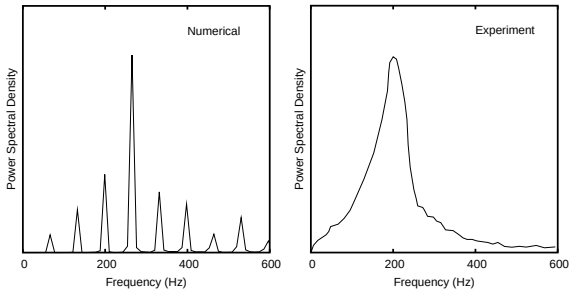

Figure 4. Transonic inlet diffuser outlet wall pressure spectrum

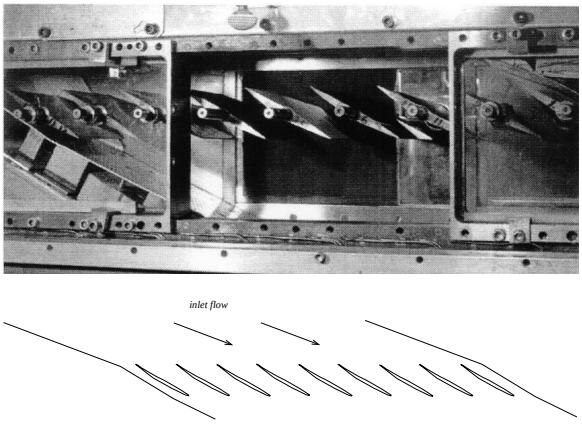

Figure 5. Test Section of the NASA Transonic Flutter Cascade [13]

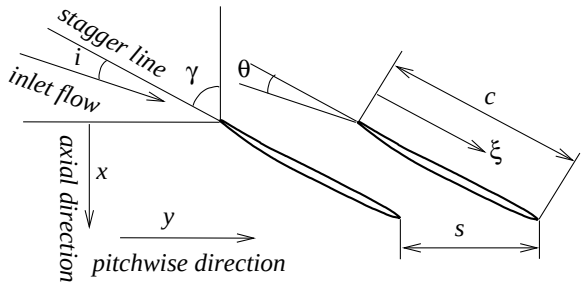

Figure 6. Cascade Structure Parameter [13]

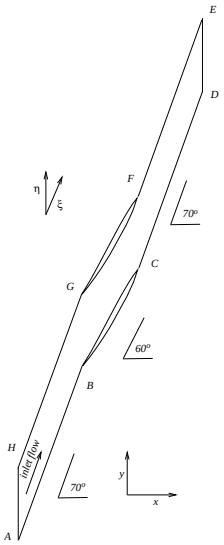

Figure 7. Cascade 2D Computation Domain

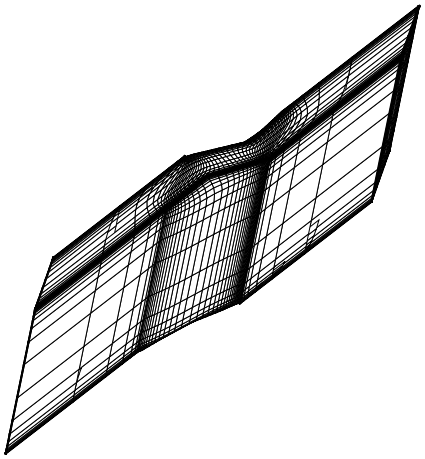

Figure 8. Cascade 3D Mesh

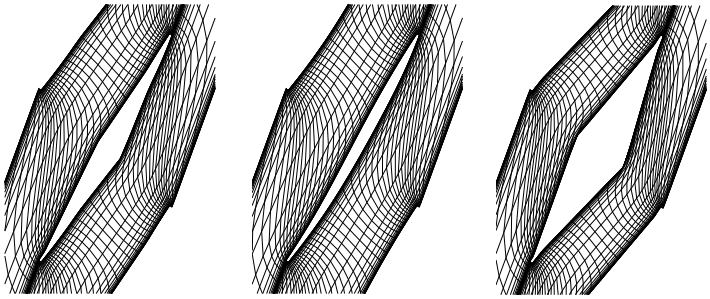

Figure 9. Cascade 2D Mesh at 3 Span-wise Planes

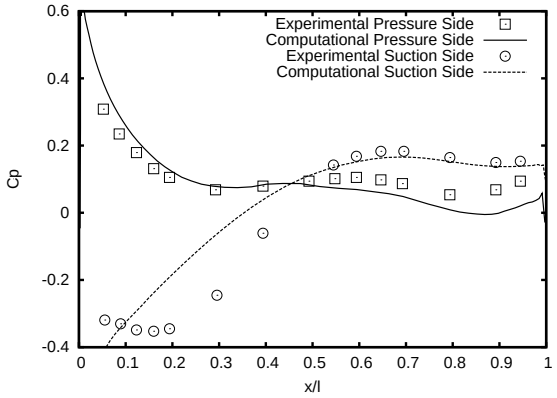

Figure 12. Mid-span Surface Pressure Distribution at Incidence Angle 10°

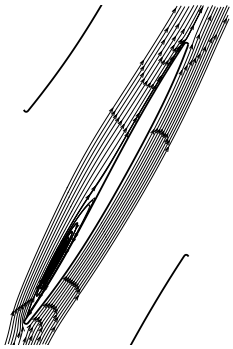

Figure 10. Mid-span Stream Lines at Incidence Angle 10°

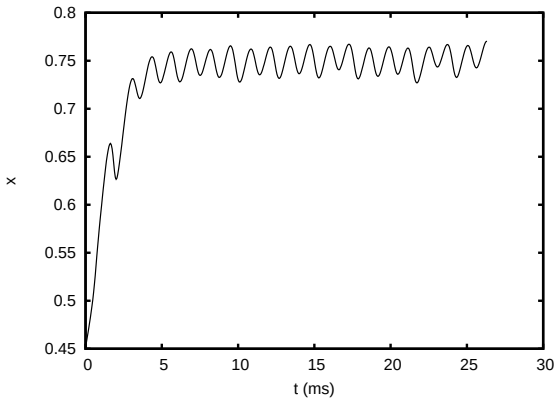

Figure 13. Separation Zone Length Variation with Time

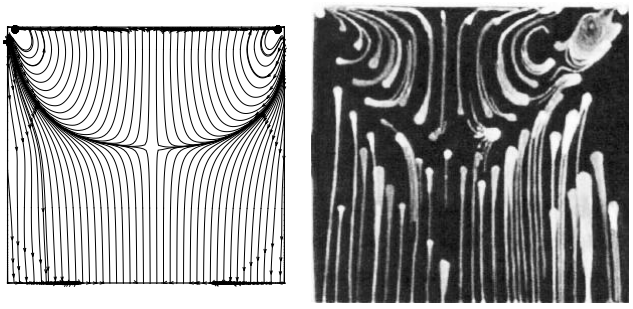

Figure 11. Mid-span Suction Surface Streamlines at Incidence Angle 10°

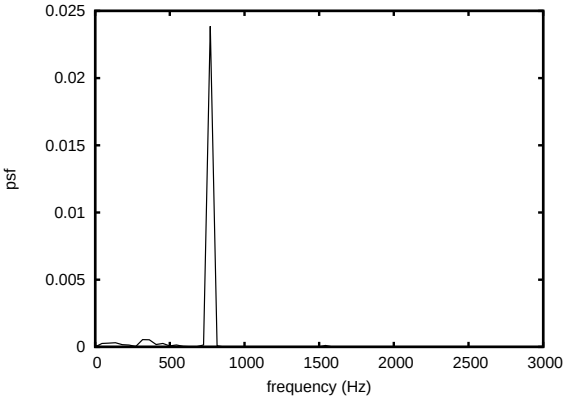

Figure 14. Separation Zone Length Variation Frequency Spectrum

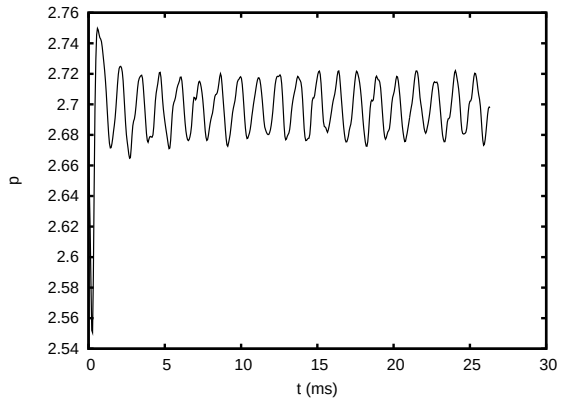

Figure 15. Suction Surface Check Point Pressure Variation with Time

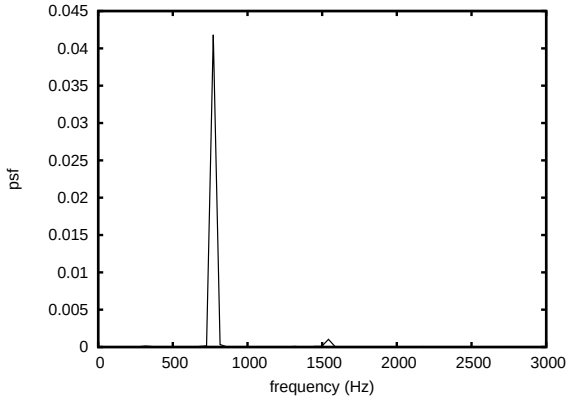

Figure 16. Suction Surface Check Point Pressure Frequency Spectrum

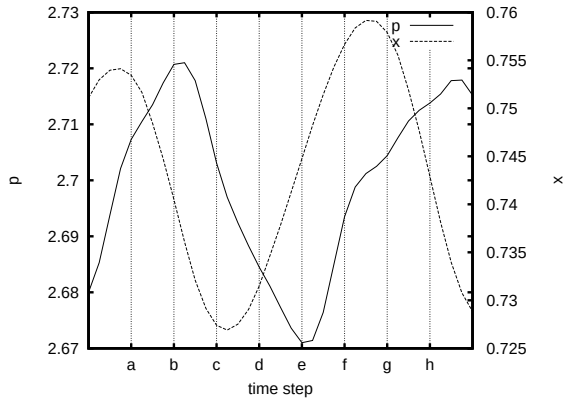

Figure 17. Check Point Pressure and Separation Locations Relation

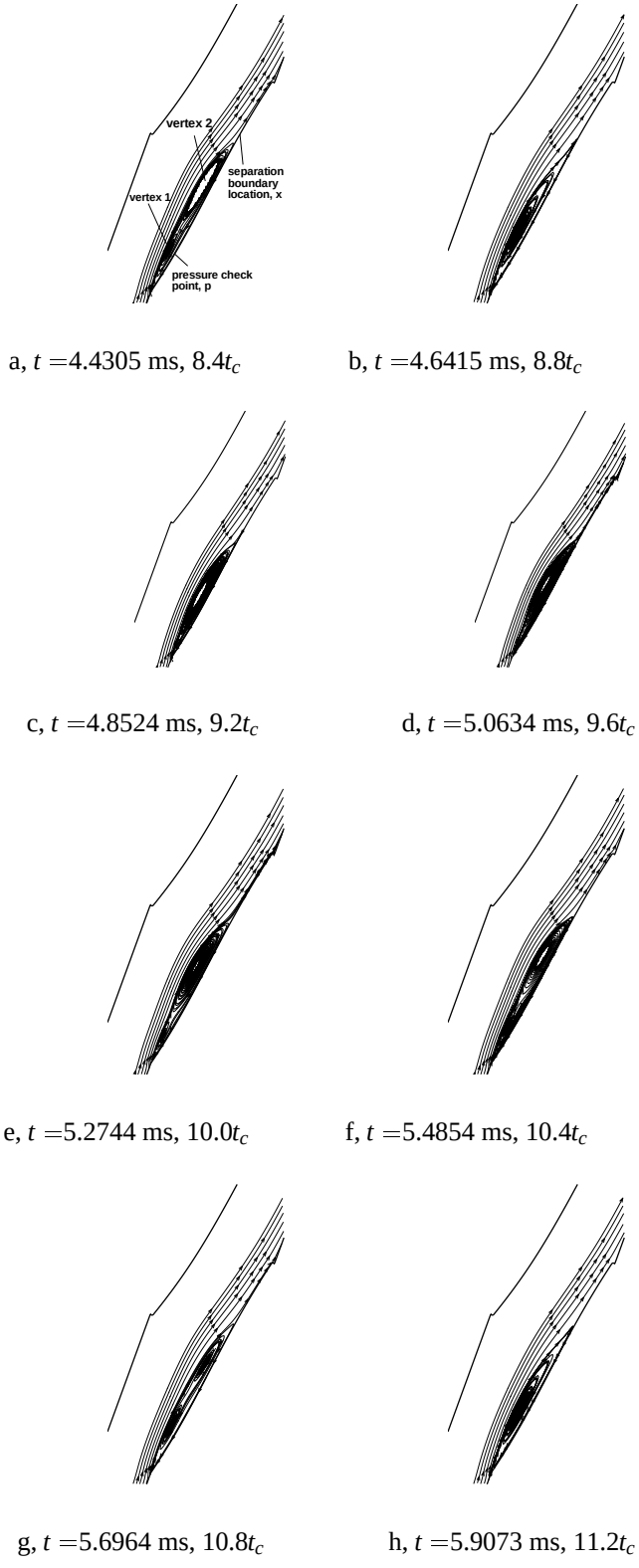

a, t =4.4305 ms, $8.4t_c$ b, t =4.6415 ms, $8.8t_c$

c, t =4.8524 ms, $9.2t_c$ d, t =5.0634 ms, $9.6t_c$

e, t =5.2744 ms, $10.0t_c$ f, t =5.4854 ms, $10.4t_c$

g, t =5.6964 ms, $10.8t_c$ h, t =5.9073 ms, $11.2t_c$

Figure 18. Separation Bubble Evolution

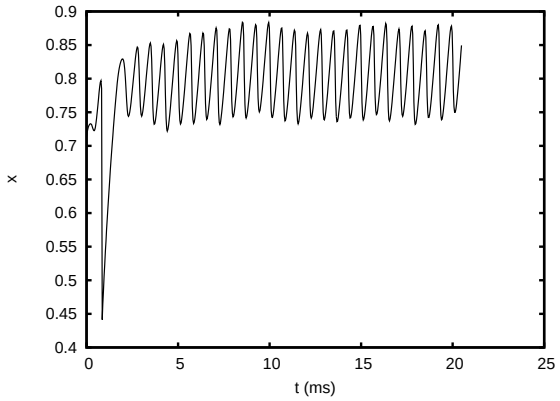

Figure 19. Separation Zone Length Oscillation (Ma=0.8)

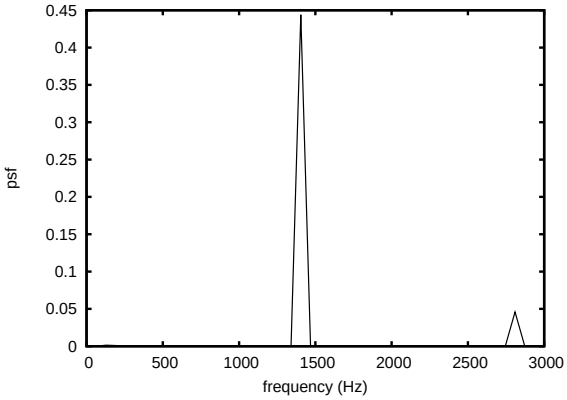

Figure 20. Separation Zone Length Oscillation Frequency Spectrum (Ma=0.8)

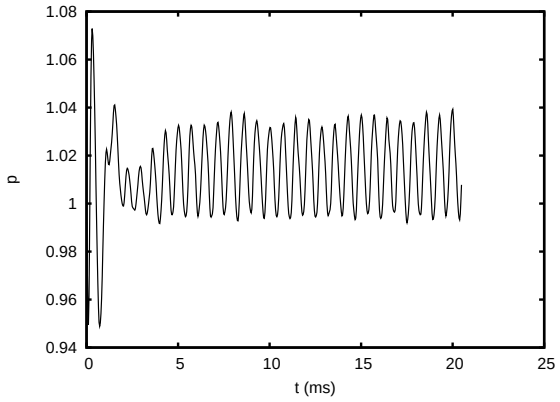

Figure 21. Checkpoint Pressure Oscillation (Ma=0.8)

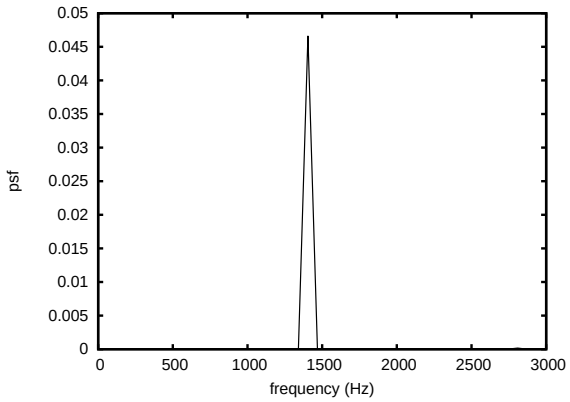

Figure 22. Checkpoint Pressure Oscillation Frequency Spectrum (Ma=0.8)

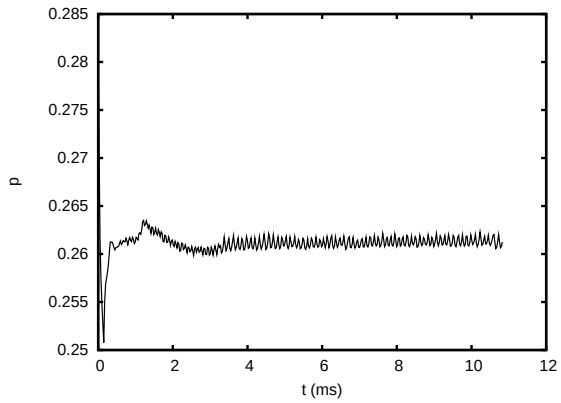

Figure 23. Checkpoint Pressure Oscillation (Ma=1.18)

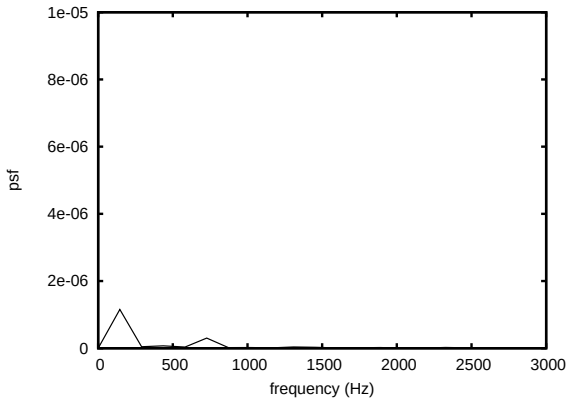

Figure 24. Checkpoint Pressure Oscillation Frequency Spectrum (Ma=1.18)